Nabaa A. Ibrahim
Suhad A. Hamdan

Department of Physics,
College of Science,
University of Baghdad,
Baghdad, IRAQ

Iraqi Journal of Applied Physics

Q4 — Electronic, Optical and Magnetic Materials
best quartile

SJR 2023
0.18
powered by scimagojr.com
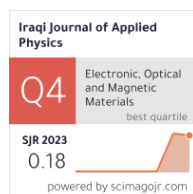
Tunable Structural and Optical Properties of Hydrothermally Synthesized Zn₁₋ₓMnₓFe₂O₄ Nanostructures

In this study, zinc-manganese ferrite ($Zn_{1-x}Mn_xFe_2O_4$) nanostructures were prepared at different Mn substitution ratios (x = 0, 0.2, 0.4) with a hydrothermal route. The structural, morphology, and optical properties of the prepared samples were studied. Results confirmed the polycrystalline nature and spinel-ferrite structure, and the crystallinity and crystallite size decreased with increasing Mn content. Spherical nanoparticles were formed with distinct levels of aggregation and porosity, relying on the Mn substitution ratio. The functional absorption bands of metallic-oxygen bonds and different molecular interactions were confirmed. A significant change in the absorption spectrum with increasing manganese content as well as an increase in the optical energy gap were osberved, indicating tunable electronic properties. The tunable structural, optical, and morphological properties of the $Zn_{1-x}Mn_xFe_2O_4$ nanostructures with different Mn contents indicate their potential application in magnetic materials, catalysis, and biomedical fields.

1. Introduction

Nanostructured materials have emerged as a critical area of scientific research owing to their unique properties and diverse applications in technological fields [1]. Among these materials, spinel ferrites have attracted significant interest for their versatile magnetic, optical, and electronic properties [2,3]. Zinc ferrite ($ZnFe_2O_4$), a notable member of the spinel ferrite family, is distinguished by its high chemical stability and tunable magnetic properties, making it suitable for a wide range of applications, including electronics, catalysis, and biomedicine [4].

Doping spinel ferrites with various metal ions is a well-established method for tailoring their structural, magnetic, and optical properties [5]. Metal substitution involves replacing Zn ions in the ferrite lattice with other metal ions, such as manganese (Mn), cobalt (Co), or nickel (Ni). This substitution can significantly alter the cation distribution between the tetrahedral (A) and octahedral (B) sites of the spinel structure, thereby influencing the material's physical properties [6]. Manganese (Mn) is frequently used as a dopant to enhance these properties because of its influence on the crystallite size, lattice parameters, and overall material properties [7]. Substituting Zn^{2+} ions with Mn^{2+} in the $ZnFe_2O_4$ lattice induces significant changes that can be exploited for advanced applications [8].

Hydrothermal synthesis is a widely used technique for producing high-purity nanostructured ferrites with controlled morphology [9,10]. This method involves high-pressure and high-temperature aqueous solutions to facilitate the formation of nanostructures, allowing precise control over the doping concentration [11,12]. Hydrothermal synthesis is particularly effective for preparing the $Zn_{1-x}Mn_xFe_2O_4$, as it enables a detailed study of how varying Mn content influences the material's properties [13,14]. Understanding the effects of dopants on spinal nanostructures is expected to provide insights that can drive the development of materials with enhanced performance for applications in optoelectronics, photocatalysis, and other fields requiring precise control of electronic and magnetic properties [15,16].

This study aims to comprehensively investigate the synthesis, structural, optical, and morphological properties of metal ferrite samples $Zn_{1-x}Mn_xFe_2O_4$ prepared via hydrothermal synthesis with various Mn contents (x).

2. Experimental Part

$Zn_{1-x}Mn_xFe_2O_4$ nanostructures were synthesized from metal nitrate precursors using a hydrothermal method. Zinc nitrate hexahydrate, ferric nitrate monohydrate, and manganese nitrate were each dissolved in distilled water to create 0.2M solutions with the help of a magnetic stirrer. Sodium hydroxide (NaOH) was dissolved in deionized water at 70 °C to form a 1M solution. The metal salt solutions were prepared using the nitrate precursors, and their weights were calculated according to the molecular weight of the salt and the ion ratio of each sample. The metal salts were gradually added to the boiling NaOH solution, and the pH was adjusted to 9. This mixture was stirred for 6 hours at 70 °C, and the result turned black. The mixture was then transferred to an autoclave and heated in an oven at 100 °C for 3 hours. The resulting solution was centrifuged at 6000 rpm for 30 min and repeated three times. The precipitate was dried at 100 °C for 30 min, resulting in a small black mass that was ground into a black powder. This powder was calcined at 600 °C to yield samples ready for characterization. The synthesis process was repeated with various Mn substitution ratios. The

structural, morphological, and optical properties of the samples were analyzed using x-ray diffraction (XRD), field-emission scanning electron microscopy (FE-SEM), Fourier-transform infrared spectroscopy (FTIR), and UV-visible spectrophotometry.

3. Results and Discussions

Figure (1) shows the XRD patterns of $ZnFe_2O_4$, $Zn_{0.8}Mn_{0.2}Fe_2O_4$, and $Zn_{0.6}Mn_{0.4}Fe_2O_4$ nanostructures synthesized by the hydrothermal route. All samples appeared to have polycrystalline peaks that matched the spinal ferrite structure according to standard JCPDS card 01-077-001. The crystallinity decreased with increasing Mn content. These results are in good agreement with previous studies [17].
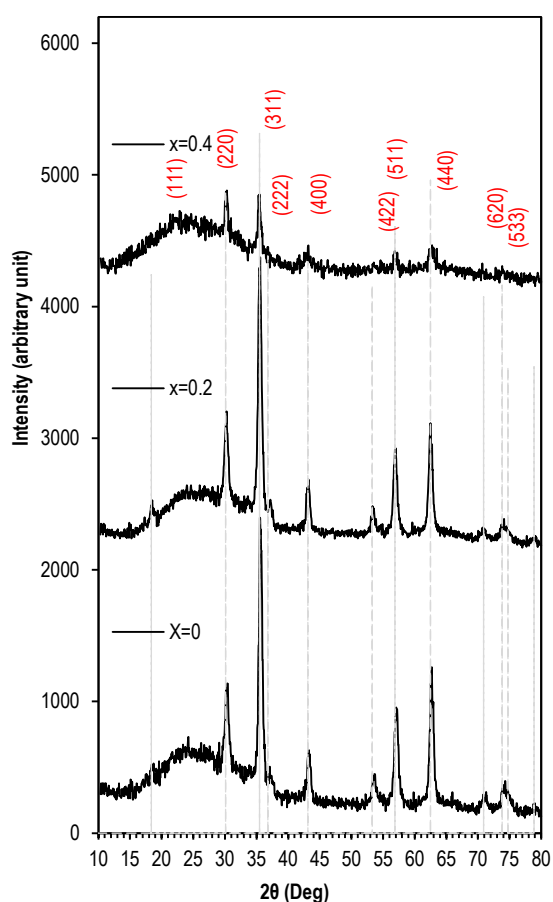

Fig. (1) XRD patterns of $Zn_{1-x}Mn_xFe_2O_4$ at different Mn substitutions

Increasing the Mn substitution content demonstrates minor shifts in the peak location toward higher 2θ, indicating a slight decrease in the lattice parameter. Lattice parameters vary depending on the type and ratio of the substituted cations, causing shifts in the diffraction peaks because of variations in the ion radius of Mn compared to Zn [18]. As shown in table (1), there was an increase in the broadening of the diffraction line, designated as a reduction in the average crystallite size with increasing Mn content [19].

The lattice parameter (*a*) was determined according to the relation corresponding to the cubic structure [20]:

$$d_{hkl} = \frac{a}{\sqrt{h^2+k^2+l^2}} \tag{1}$$

Table (2) lists the variations in lattice parameter (*a*), which increased by 8.3514, 8.3587, and 8.3606 Å for x=0, 0.2, and 0.4, respectively. These values agree with a previously reported lattice parameter for spinal zinc ferrite [21].

The close-packing lattice density of the prepared $Zn_{1-x}Mn_xFe_2O_4$ structure was determined by the formula [22]:

$$\rho_x = \frac{n\,M_w}{N_A\,a^3} \tag{2}$$

Here, *n* is the number of molecules per unit cell, which equals 8 for a spinal ferrite structure [23], N_A is Avogadro's number, and M_w is the molecular weight

The ion jump lengths at the tetrahedral site (L_A) and octahedral site (L_B) were determine according to the lattice parameter [24]:

$$L_A = \frac{\sqrt{3}a}{4} \quad \text{and} \quad L_B = \frac{\sqrt{3}a}{2} \tag{3}$$

Table (2) shows the variations in the lattice parameter (*a*), lattice volume (*V*), close packing density (ρ_x), L_A, and L_B. It seems that the L_A and L_B increase directly with the substitution ratio due to the difference in Mn and Zn ionic radii [25].

Table (2) Lattice constants (a), lattice volumes (V), density (ρ_x), and ion jump lengths (L_A, L_B) of $Zn_{1-x}Mn_xFe_2O_4$ at different values of x

x	a (Å)	V (Å)^3	ρ (g/cm^3)	L_A	L_B
0	8.3514	582.476	5.260	3.616	7.233
0.2	8.3587	584.005	5.294	3.619	7.239
0.4	8.3606	584.403	5.338	3.62	7.240

Figure (2) shows the FE-SEM images of $ZnFe_2O_4$, $Zn_{0.8}Mn_{0.2}Fe_2O_4$, and $Zn_{0.6}Mn_{0.4}Fe_2O_4$ samples prepared by the hydrothermal route. The surface of the $ZnFe_2O_4$ sample appeared as a porous structure formed from attached spherical nanoparticles of uniform size across all samples with a diameter of approximately 60 nm.

Sample $Zn_{0.8}Mn_{0.2}Fe_2O_4$ was also composed of aggregated nanoparticles of nearly spherical shape but with smaller dimensions (~ 20 nm diameter). The nanoparticles appeared more aggregated with each other. The increased aggregation may lead to variations in different properties, such as magnetic properties, due to interactions between particles. The aggregation may affect optical properties. In addition, aggregation can reduce the available surface area, leading to decreased chemical reactivity and catalytic efficiency. In $Zn_{0.6}Mn_{0.4}Fe_2O_4$, the average particle diameter was 25 nm, and the particles were composed of spherical nanoparticles of lower particle size. Reduce particle size with low aggregation and high area-to-volume ratio, resulting in enhanced surface area, which leads to improved capability for use in catalysis or biomedical imaging.
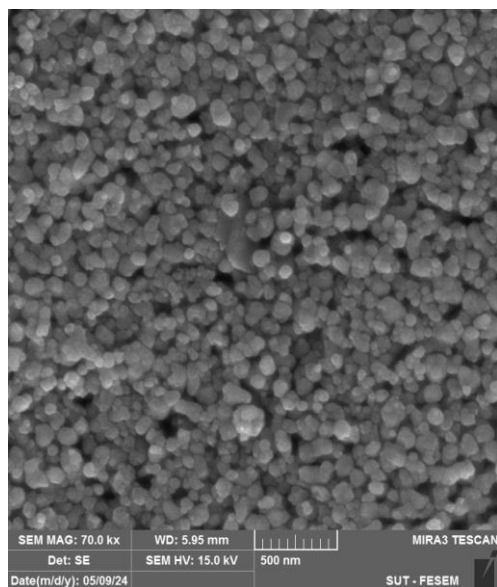
X=0
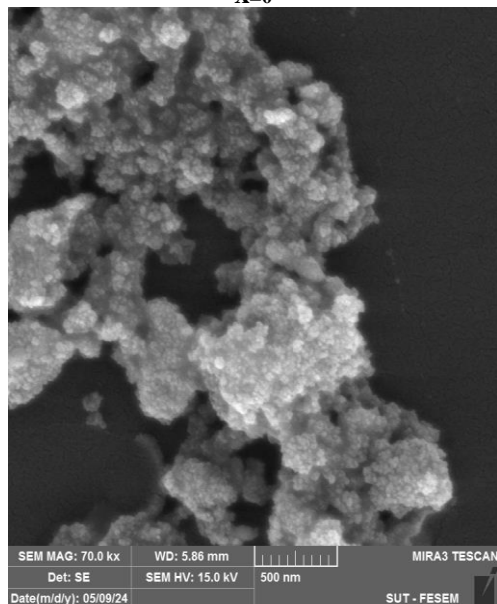
X=0.2
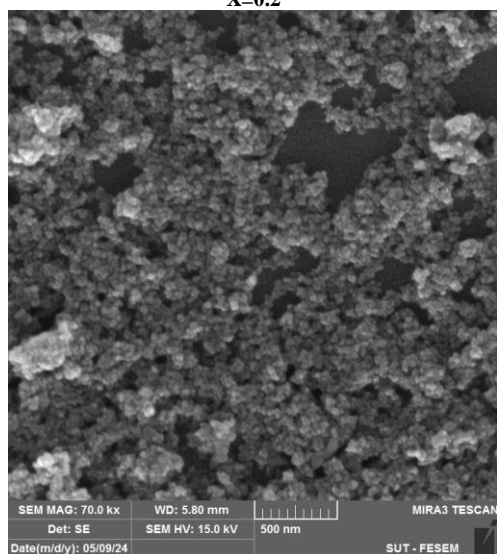
X=0.4

Fig. (2) FE-SEM images of $Zn_{1-x}Mn_xFe_2O_4$ at different Mn substitutions

Figure (3) presents the FTIR transmission spectra of $Zn_{1-x}Mn_xFe_2O_4$ prepared by the hydrothermal method within the 400-4000 cm^{-1} range at different Mn-Zn substitution ratios. All spinel ferrites exhibited two significant absorption bands in the 400 to 700 cm^{-1} wavenumber range. The band around 565 cm^{-1} wavenumber bands corresponding to the vibrations of the metal oxide (Fe^{3+}-O^{2-}) at the tetrahedral site (site A), while the band with lower energy around 450 cm^{-1} wavenumber corresponding to octahedral metal-oxide stretching (site B). The two bands of the $ZnFe_2O_4$ differ in energy due to different sites with different M-O distances between the octahedral and tetrahedral sites [26]. The appearance of these bands indicates the synthesis of a spinel ferrite structure, which is consistent with the determined ion jump length values [27].
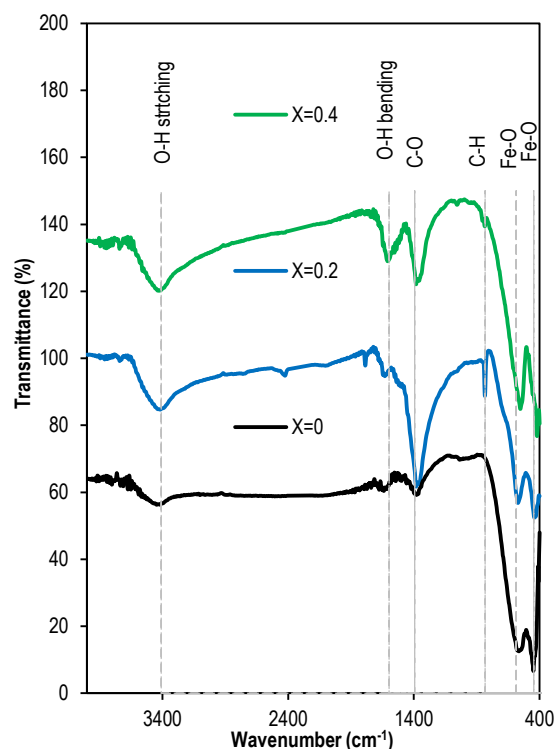

Fig. (3) FTIR spectra of $Zn_{1-x}Mn_xFe_2O_4$ samples prepared with different Mn substitutions

Table (3) FTIR bands of $Zn_{1-x}Mn_xFe_2O_4$ samples prepared with different Mn substitutions

Band type	X=0	X=0.2	X=0.4
O-H stretching	3435.57	3421.53	3427.15
O-H bending	1629.95	1629.85	1607.49
C-O	1380.03	1365.99	1371.61
C-H	-	835.26	832.45
Fe-O	565.68	562.30	554.64
Fe-O	450.55	436.51	425.66

The band that appeared at 1600 cm^{-1} corresponded to the bending mode of O-H, indicating the existence

of some water molecules, while the band seen at 2220 cm^{-1} corresponds to the C≡C band of aromatic compounds. These strange bands adsorbed from ambient, in the sample of x=0.2, resulting from variations in sample porosity.

The absorption bands around 3435 and 1629 cm^{-1} correspond to the stretching and vibration modes of the O−H band, respectively [28]. The absorption bands around 1380 and 835 cm^{-1}, as shown in table (3), correspond to C-O vibration and C-H bending, respectively, and come from the residual elements of the preparation precursors [29].

The substitution of Mn^{+2} instead of Zn^{+2} in the $Zn_{1-x}Mn_xFe_2O_4$ lattice and its increasing ratio caused a shift of the prominent bands toward lower wavenumbers, indicating a reduction in the band energy as a result of increasing the bond length (L_A and L_B) [30]. Additionally, increasing the Mn substitution ratio reduced the intensity of the main band, indicating a reduction in the crystallinity of the sample. The variation in the C-O band intensity from sample to sample and the absence of C-H vibrations in the sample of x=0, while present in other samples, indicates different contents of carbonyl groups, resulting from the variation in sample porosity, which causes the sample to adsorb different amounts of gas molecules from the ambient environment.

The optical properties of $Zn_{1-x}Mn_xFe_2O_4$ samples prepared at different Mn-Zn substitution ratios were analyzed using UV-visible spectrophotometry, covering wavelengths from 300 to 1100 nm. The analysis revealed significant changes in the absorbance spectra with increasing Mn substitution ratio. Figure (4) shows the optical absorption spectra and Tauc plots, which were applied to determine the optical energy gaps of the spinal ferrite samples. The absorbance of all samples increased with decreasing wavelength, with a notable increase at the absorption edge at approximately 500nm. This behavior is typical of semiconductors, where the material absorbs more light at shorter wavelengths due to the higher-energy photons being absorbed to excite electrons from the valence band to the conduction band. The samples exhibited low absorbance, indicating that the materials are less interactive at longer wavelengths.

This property may be exploited in applications requiring transparency in the IR area. The absorption edge was blue-shifted with increasing Mn substitution ratio, showing an increment in the optical bandgap because the Mn content increased. This alternate is probably because of the one of a kind digital configuration and influence of Mn ions compared to Zn ions, which affect the electronic shape of the ferrite. The observed blue shift inside the absorption area with extended Mn substitution suggests that the band gap of these substances may be tuned by adjusting the Mn content, improving their photocatalytic interest below UV light and making these ferrites versatile for numerous technological applications.

Tauc plots of $(\alpha h\upsilon)^2$ versus the photon energy (hυ) are used to estimate the bandgap energy of the samples. The intercept of the extrapolated linear part of this plot with the x-axis gives the material's optical bandgap (E_g) [31]. The determined optical bandgaps increase with increasing Mn content (x = 0, 0.2, and 0.4) to 1.8, 1.9, and 2.0 eV, respectively. This increase in bandgap energy upon substituting Zn with Mn can be attributed to changes in the material's electronic structure due to the distinct electronic configurations of Mn and Zn ions. As the Mn content increases, the electronic interactions within the ferrite lattice are altered, leading to a higher energy required to excite an electron from the valence band to the conduction band. The increased bandgap energy with increasing Mn substitution has significant implications for the optical properties and potential applications of these ferrite materials. For example, materials with larger bandgaps are often more suitable for optoelectronics and photocatalytic applications.
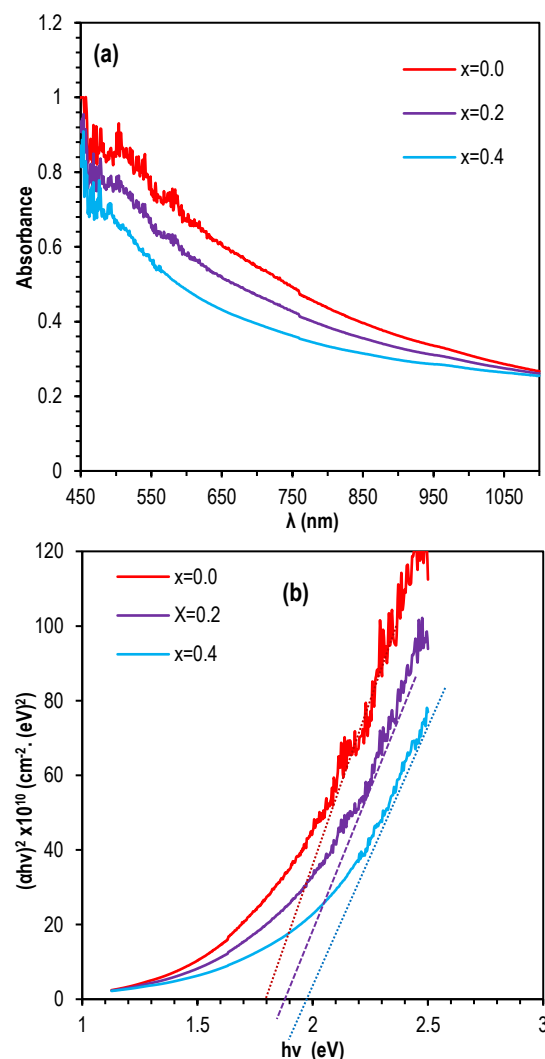

Fig. (4) Absorption spectra of $Zn_{1-x}Mn_xFe_2O_4$ samples at different x values (a) and their Tauc plots (b)

4. Conclusions

In this work, $Zn_{1-x}Mn_xFe_2O_4$ nanostructures were successfully synthesized at x = 0, 0.2, and 0.4 by the hydrothermal route. The polycrystalline spinel ferrite structure was confirmed by observing reduced crystallinity, decreased crystallite size, and a slight decrease in lattice parameter with increasing Mn content. Variations in surface morphology, including increased aggregation, were observed at higher Mn contents, affecting the optical properties. The optical bandgap increased with increasing Mn content. The ability to tune the crystallite size, aggregation behavior, and bandgap by adjusting the Mn content in the ferrite samples allows for the customization of materials for specific technological applications, enhancing their applicability in numerous fields.

References

[1] N. Baig, I. Kammakakam and W. Falath, Nanomaterials: a review of synthesis methods, properties, recent progress, and challenges", *Mater. Adv.*, 2 (2021) 1821–1871.

[2] H. Qin et al., "Spinel ferrites (MFe_2O_4): Synthesis, improvement and catalytic application in environment and energy field", *Adv. Colloid Interface Sci.*, 294 (2021) 102486.

[3] A.J. Raheem and S.M. Raji, "Nickel Ferrite Nanostructures Prepared by DC Reactive Magnetron Sputtering", Iraqi J. Appl. Phys. Lett., 7(2) (2024) 7-10.

[4] P. Sahoo et al., "Recent advances in zinc ferrite ($ZnFe_2O_4$) based nanostructures for magnetic hyperthermia applications", *Chem. Commun.*, 59 (2023) 12065–12090.

[5] Sonia et al., "Spinel ferrites/metal oxide nanocomposites for waste water treatment", *Appl. Phys. A,* 129 (2023) 91.

[6] B. Issa et al., "Magnetic nanoparticles: Surface effects and properties related to biomedicine applications", *Int. J. Mol. Sci.*, 14 (2013) 21266–21305.

[7] P. Monisha et al., "Influence of Mn dopant on the crystallite size, optical and magnetic behaviour of $CoFe_2O_4$ magnetic nanoparticles", *J. Phys. Chem. Solids,* 148 (2021) 109654.

[8] N.A. Jasim, S.E. Ebrahim and S.H. Ammar, "Fabrication of $Zn_xMn_{1-x}Fe_2O_4$ metal ferrites for boosted photocatalytic degradation of Rhodamine-B dye", *Results Opt.*, 13 (2023) 100508.

[9] A.L. Gurgel et al., "Microwave-assisted hydrothermal synthesis and magnetic properties of nanostructured cobalt ferrite", *J. Alloys Comp.,* 799 (2019) 36–42.

[10] S. Hoghoghifard, and M. Moradi, "Influence of annealing temperature on structural, magnetic, and dielectric properties of $NiFe_2O_4$ nanorods synthesized by simple hydrothermal method", *Ceram. Int.*, 48 (2022) 17768–17775.

[11] W. Shi, S. Song and H. Zhang, "Hydrothermal synthetic strategies of inorganic semiconducting nanostructures", *Chem. Soc. Rev.*, 42 (2013) 5714–5743.

[12] N. Wiriya et al., "Magnetic properties of $Zn_{1-x}Mn_xFe_2O_4$ nanoparticles prepared by hydrothermal method", *Microelectro. Eng.*, 126 (2014) 1-8.

[13] Y.X. Gan et al., "Hydrothermal Synthesis of Nanomaterials", *J. Nanomater.*, 2020 (2020) 1–3.

[14] A. Ashok, L. John Kennedy and J. Judith Vijaya, "Structural, optical and magnetic properties of $Zn_{1-x}Mn_xFe_2O_4$ $(0 \le x \le 0.5)$ spinel nano particles for transesterification of used cooking oil", *J. Alloys Comp.*, 780 (2019) 816-828.

[15] F. Gao et al., "Preparation of magnetic $ZnFe_2O_4$ nanosphere photocatalyst for high concentration ammonia nitrogen wastewater treatment", *J. Environ. Chem. Eng.*, 11 (2023) 110894.

[16] Ö. Yavuz, M.K. Ram and M. Aldissi, "Chapter 9 - Electromagnetic applications of conducting and nanocomposite materials", V. Erokhin, M. Kumar Ram and O. Yavuz (ed.), The New Frontiers of Organic and Composite Nanotechnology, Elsevier (2008), pp. 435-475,

[17] T.S. Algarni et al., "Activated Carbon/$ZnFe_2O_4$ Nanocomposite Adsorbent for Efficient Removal of Crystal Violet Cationic Dye from Aqueous Solutions", *Nanomaterials*, 12 (2022) doi: 10.3390/nano12183224.

[18] L. Pauling, "The sizes of ions and the structure of ionic crystals", *J. Am. Chem. Soc.*, 49 (1927) 765–790.

[19] F. Tudorache et al., "Studies on the structure and gas sensing properties of nickel–cobalt ferrite thin films prepared by spin coating", *Mater. Sci. Eng. B,* 178 (2013) 1334-1338.

[20] A.J. Dekker, **"Solid State Physics"**, MacMillan & Co., Ltd. (London, 1958), p. 10.

[21] J.P. Singh et al., "^{57}Fe Mössbauer spectroscopic study of nanostructured zinc ferrite", *Hyperfine Interact.*, 183 (2008) 221–228.

[22] R. Creese, **"Introduction to Manufacturing Processes and Materials"**, CRC Press (2017), p. 40.

[23] A.R. Chavan et al., "Effect of Annealing Temperature on Structural, Morphological, Optical andMagnetic Properties of $NiFe_2O_4$ Thin Films", *J. Supercond. Nov. Magn.*, 31 (2018) 2949–2958.

[24] A. Verma and V.K. Jain, **"Physics of Semiconductor Devices"**, Springer International Publishing (2013), p. 66.

[25] R. Tiwaria et al., "Structural and magnetic properties of tailored $NiFe_2O_4$ nanostructures synthesized using auto-combustion method", *Results Phys.*, 16 (2020) 102916.

[26] M. Khan, **"Ferrites Synthesis and Applications"**, IntechOpen (2021).

[27] Y. Iqbal, H. Bae and I. Rhee, "Relaxivities of

Hydrogen Protons in Aqueous Solutions of PEG-coated Rod-shaped Manganese-Nickel-Ferrite ($Mn_{0.4}Ni_{0.6}Fe_2O_4$) Nanoparticles", *J. Korean Phys. Soc. Relaxivities,* 65 (2014) 1594–1597.

[28] J.P. Hemaunt Kumar et al., "FTIR and Electrical Study of Dysprosium Doped Cobalt Ferrite Nanoparticles", *J. Nanosci.*, 2014 (2014) 1–10.

[29] M.S. Lashkenari et al., "Synthesis and characterization of polyrhodanine/nickel ferrite nanocomposite with an effective and broad spectrum antibacterial activity", *Polym. Technol. Mater.*, 58 (2019) 1–10.

[30] S. Munir et al., "Nickel ferrite/zinc oxide nanocomposite: Investigating the photocatalytic and antibacterial properties", *J. Saudi Chem. Soc.*, 25 (2021) 101388.

[31] J. Singh, **"Optical Properties of Condensed Matter and Applications"**, John-Wiley & Sons, Inc. (UK, 2006), p. 49.

Table (1) Diffraction angle and crystallite size of $Zn_{1-x}Mn_xFe_2O_4$ at different values of x in different directions

x	2θ (deg)					Crystallite size (nm)			
	(220)	(311)	(511)	(440)		(220)	(311)	(511)	(440)
0.0	30.3047	35.5908	57.1481	62.7262		13.5	17.7	14.0	13.3
0.2	30.2988	35.5607	56.9946	62.5948		11.3	17.4	13.5	12.7
0.4	30.2971	35.5561	56.9681	62.5270		10.4	13.8	12.8	11.3